



Physical properties of centaur (54598) Bienor from photometry

E. Fernández-Valenzuela,^{*} J. L. Ortiz, R. Duffard, N. Morales and P. Santos-Sanz

Instituto de Astrofísica de Andalucía, CSIC, Glorieta de la Astronomía s/n, E-18008 Granada, Spain

Accepted 2016 December 13. Received 2016 December 12; in original form 2016 August 2

ABSTRACT

We present time series photometry of Bienor in four observation campaigns from 2013 to 2016 and compare them with previous observations in the literature dating back to 2000. The results show a remarkable decline in the amplitude of the rotational light curve and in the absolute magnitude. This suggests that the angle between the rotation axis and the line of sight has changed noticeably during the last 16 yr as Bienor orbits the Sun. From the light-curve amplitude data, we are able to determine the orientation of the rotation axis of Bienor ($\beta_p = 50 \pm 3^\circ$, $\lambda_p = 35 \pm 8^\circ$). We are also able to constrain the b/a axial ratio of a triaxial Jacobi ellipsoidal body (with semi-axis $a > b > c$). The best fit is for $b/a = 0.45 \pm 0.05$, which corresponds to a density value of $594^{+47}_{-35} \text{ kg m}^{-3}$ under the usual assumption of hydrostatic equilibrium and given that Bienor's rotational period is 9.17 h. However, the absolute magnitude of Bienor at several epochs is not well reproduced. We tested several explanations such as relaxing the hydrostatic equilibrium constraint, a large north–south asymmetry in the surface albedo of Bienor or even a ring system. When a ring system of similar characteristics to those of Chariklo and Chiron is included, we can fit both the light-curve amplitude and absolute magnitude. In this case, the derived axial ratio is modified to $b/a = 0.37 \pm 0.10$. The implied density is $678^{+209}_{-100} \text{ kg m}^{-3}$. Also, the existence of a ring is consistent with the spectroscopic detection of water ice on Bienor. Nevertheless, the other explanations cannot be discarded.

Key words: techniques: photometric – Kuiper belt objects: individual: Bienor – planets and satellites: rings – planetary systems.

1 INTRODUCTION

Centaur are objects with orbits located between Jupiter's and Neptune's orbits. These bodies originally came from the Trans-Neptunian Belt and were injected to the inner part of the Solar system as a result of planetary encounters, mostly with Neptune. Accordingly, centaurs are dynamically evolved objects with unstable orbits; their lifetime is around 2.7 Myr (Horner, Evans & Bailey 2004a), and most of them may become short-period comets (Horner, Evans & Bailey 2004b; Jewitt, Morbidelli & Rauer 2008). The first centaur to be discovered was Chiron, the second largest known to date. So far, we have evidence of only the existence of about a hundred of them, compared to the thousands of Trans-Neptunian Objects (TNOs) catalogued to date, which makes them even more unique. Centaurs and TNOs are possibly the least evolved objects of the Solar system, regarding the physical properties of their materials, due to the vast distances that separate them from the Sun; they are nevertheless collisionally evolved (Campo Bagatin &

Benavidez 2012). Hence, centaurs yield important information about the formation of the Solar system and its outer part.

At present, the interest in centaurs has considerably increased since the discovery of orbiting material shaped in the form of rings around two of them, Chariklo (Braga-Ribas et al. 2014) and Chiron (Ortiz et al. 2015). One of the proposed scenarios for the formation of rings in centaurs is the collision with other bodies of around 10 km of effective diameter during their dynamic evolution from the Trans-Neptunian Belt across to the Neptune's orbit, although there might be other possible mechanisms (Hyodo et al. 2016; Pan & Wu 2016).

Bienor is one of the largest centaurs known to date besides the two aforementioned centaurs, and all 200-km sized TNOs are thought to be collisionally evolved bodies (Campo Bagatin & Benavidez 2012); therefore, it is plausible that centaurs in this size range share similar collisional and dynamical histories. Hence, Bienor may be expected to display similar properties to Chariklo and Chiron, thus the special interest raised by this object. As a result, a detailed study on Bienor's rotational light curves along with its absolute magnitude has been carried out in this work. Bienor was initially designated as 2000 QC₂₄₃, and it was discovered, as its name indicates, in the year 2000. Since then, observational data

^{*} E-mail: estela@iaa.es

Table 1. Journal of observations of Bienor from different telescopes. The *R* and *V* filters are based on the Bessell system and the *r*_SDSS filter is based on the Sloan Digital Sky Survey. Abbreviations are defined as follows: exposure time (T_E); number of images (N) and time on target each night (T_{obj}).

Date	Telescope	Filter	Binning	Seeing (arcsec)	T_E (s)	N	T_{obj} (h)
2013 Dec 6	OSN 1.5 m	<i>V</i>	2×2	1.89	500	3	0.42
2013 Dec 6	OSN 1.5 m	<i>R</i>	2×2	2.11	500	2	0.28
2014 Nov 18	CAHA 1.23 m	Clear	2×2	1.72	300	21	1.75
2014 Nov 19	CAHA 1.23 m	Clear	2×2	1.61	300	22	1.83
2014 Dec 18	CAHA 1.23 m	Clear	2×2	1.84	300	26	2.17
2014 Dec 27	NOT	<i>R</i>	1×1	1.08	250	63	4.37
2014 Dec 28	NOT	<i>R</i>	1×1	0.94	250	56	3.89
2015 Nov 5	CAHA 1.23 m	Clear	2×2	1.44	250	41	2.85
2015 Nov 6	CAHA 1.23 m	Clear	2×2	1.46	250	75	5.21
2015 Dec 13	NOT	<i>r</i> _SDSS	1×1	0.74	400	10	1.11
2016 Aug 4	OSN 1.5 m	<i>R</i>	2×2	1.77	300	22	1.83
2016 Aug 5	OSN 1.5 m	<i>R</i>	2×2	1.91	400	15	1.67
2016 Aug 6	OSN 1.5 m	<i>R</i>	2×2	1.70	400	21	2.33
2016 Aug 7	OSN 1.5 m	<i>R</i>	2×2	2.51	400	18	2.00
2016 Aug 8	OSN 1.5 m	<i>R</i>	2×2	1.79	400	19	2.11
2016 Aug 5	OSN 1.5 m	<i>V</i>	2×2	1.91	400	4	0.45
2016 Aug 7	OSN 1.5 m	<i>V</i>	2×2	2.51	400	7	0.78
2016 Aug 8	OSN 1.5 m	<i>V</i>	2×2	1.79	400	4	0.45

Table 2. Colours of the Landolt standard stars used for calibrations during campaigns 2013 and 2016.

Campaign	Colour	PG2213+006A		PG2213+006B		PG2213+006C	
2013	$V - R$	0.406 ± 0.003		0.4270 ± 0.0008		0.4260 ± 0.0023	
	$R - I$	0.403 ± 0.005		0.4020 ± 0.0015		0.4040 ± 0.0068	
	Colour	SA23_433	SA23_435	SA23_438	SA23_440	SA23_443	SA23_444
2016	$V - R$	0.386 ± 0.003	0.4690 ± 0.0013	0.5110 ± 0.0014	0.4930 ± 0.0029	0.3680 ± 0.0007	0.5500 ± 0.0065
	$R - I$	0.3680 ± 0.0013	0.4760 ± 0.0013	0.5140 ± 0.0049	0.4640 ± 0.0012	0.3690 ± 0.0007	0.5140 ± 0.0105

Table 3. Colours of Bienor from data published in this work and previous literature.

Colour	2000 Nov. ^a	2001 Aug. ^b	2002 ^{c,f}	2002 Aug. ^d	2013 Oct. ^e	2016 Aug. ^e
<i>V</i> – <i>R</i>	0.45 ± 0.04	0.44 ± 0.03	0.38 ± 0.06	0.48 ± 0.04	0.42 ± 0.07	0.44 ± 0.07
<i>R</i> – <i>I</i>	0.40 ± 0.07	0.47 ± 0.03	0.41 ± 0.06	0.58 ± 0.06		

^aDelsanti et al. (2001). ^bDoressoundiram et al. (2002). ^cBauer et al. (2003). ^dDoressoundiram et al. (2007). ^eThis work.^fBauer et al. (2003) observed Bienor on 2001 October 29 and on 2002 June 13.

were published in numerous studies on colours, absolute magnitude and other photometric and spectroscopic data (e.g. Delsanti et al. 2001; Ortiz et al. 2002; Dotto et al. 2003; Romanishin & Tegler 2005). However, many aspects remained to be studied.

Here, we present an extensive study of this object from the photometric point of view. Observations and data reduction are detailed in Section 2. These results are not satisfactory reproducing the variation of the absolute magnitude at different epochs. Diverse scenarios that might overcome this issue are studied in Sections 5.3, 5.4 and 5.5. A general discussion is presented in Section 6. Section 7 closes the paper with a brief summary.

2 OBSERVATIONS AND DATA REDUCTION

We carried out four observation campaigns between 2013 and 2016 using different telescopes. A log of the observations is shown in Table 1. The first observation run was executed on 2013 December 6

with the 1.5-m telescope at the Sierra Nevada Observatory (OSN) in Granada, Spain, in order to obtain Bienor’s absolute magnitude. We used the 2k×2k CCDT150 camera, which has a field of view of 7.1 arcmin×7.1 arcmin and an image scale of 0.232 arcsec pixel^{−1}. The images were obtained using *V* and *R* bands in the Bessell’s filters system and in 2×2 binning mode. We calibrated the observations with the Landolt PG2213+006 field, specifically with the PG2213+006a, PG2213+006b and PG2213+006c Landolt standard stars, which share similar colours with Bienor (see Tables 2 and 3). We took 12 images of the Landolt field and 3 images of Bienor altogether in each filter (we rejected one Bienor’s *R*-band image due to blending with a star). The Landolt stars were observed at different air masses with the aim of correcting the measurements from atmospheric extinction.

The second and third observation campaigns were executed in order to obtain different rotational light curves within an approximate interval of a year between each other. The runs of the 2014

campaign took place on November 18 and 19 and December 18, 27 and 28 with the Centro Astronómico Hispano Alemán (CAHA) 1.23-m telescope of the Calar Alto Observatory in Almería (Spain) and the 2.5-m Nordic Optical Telescope (NOT) at Roque de los Muchachos in La Palma (Spain). The instrument used at the CAHA 1.23-m telescope was the 4k×4k CCD DLR-III camera. This device has a field of view of 21.5 arcmin × 21.5 arcmin and an image scale of 0.314 arcsec pixel⁻¹. No filter was used in order to obtain the largest signal-to-noise ratio (SNR). The images were dithered over the detector to prevent problems in the photometry associated with bad pixels or CCD defects. The instrument used at NOT was the 2k×2k ALFOSC camera (Andalucía Faint Object Spectrograph and Camera), with a field of view and an image scale of 6.4 arcmin × 6.4 arcmin and 0.19 arcsec pixel⁻¹, respectively. The images were obtained using the *R*-band filter in the Bessell system. A total of 188 science images were taken during the whole campaign. On the other hand, the third campaign took place on 2015 November 5 and 6 and December 13 with the same telescopes and cameras used during the 2014 campaign. No filter was used in the DLR-III camera, and *r*_SDSS (Sloan Digital Sky Survey) filter was used in ALFOSC. A total of 126 science images were taken during this campaign.

The last observation campaign took place from 2016 August 4 to 8 with the 1.5-m telescope at the OSN in Granada (Spain) in order to obtain Bienor's absolute magnitude and rotational light curve. The CCD camera was the same as in the first campaign. The images were obtained using *V* and *R* bands in the Bessell's filters system and in 2 × 2 binning mode. A total of 95 *R* band and 15 *V* band science images were taken during the whole campaign. We calibrated the observations with the Landolt SA23 field, specifically with the SA23_435, SA23_438, SA23_443, SA23_444, SA23_440 and SA23_433 Landolt standard stars, which share similar colours with Bienor (see Tables 2 and 3). Three images of the Landolt field were taken altogether in each filter. Bienor was observed at different air masses with the aim of correcting the measurements from atmospheric extinction.

When the time spent between observations made it possible, we aimed the telescope at the same region of the sky each night in order to keep fixed the same stellar field. This is convenient as it would permit to choose the same set of reference stars for all nights in the observing runs in order to minimize systematic photometric errors. At the beginning of each observation night, we took bias frames and twilight sky flat-field frames to calibrate the images. We subtracted a median bias and divided by a median flat-field corresponding to each night. Specific routines written in Interactive Data Language (IDL) were developed for this task. The routines also included the code to perform the aperture photometry of all reference stars and Bienor. The procedures we followed were identical to those described in Fernández-Valenzuela et al. (2016).

We tried different apertures in order to maximize the SNR on the object for each night and to minimize the dispersion of the photometry. We also selected a radius for the sky subtraction annulus and the width of the annulus (see Table 4).

3 RESULTS FROM OBSERVATIONS

3.1 Rotational light curves from relative photometry

We chose the same reference stars set within each observation run. All the stars showed a good photometric behaviour. We picked out stars that presented a wide range of brightness, and that were either brighter or fainter than the object, with the aim of studying the dispersion given by the photometric data of the object with regard

Table 4. Parameters of the photometric analysis. Abbreviations are defined as follows: aperture radius (aper.); radius of the internal annulus for the subtraction of the sky background (an.); width of the subtraction annulus (*d*_{an.}) and number of reference stars (*N*_{*}).

Date	aper. (pixels)	an. (pixels)	<i>d</i> _{an.} (pixels)	<i>N</i> _*
2013 Dec 6 (<i>V</i> Band)	4	15	4	3†
2013 Dec 6 (<i>R</i> Band)	4	10	4	3†
2014 Nov 18	3	13	5	13
2014 Nov 19	3	13	5	13
2014 Dec 18	3	12	5	12
2014 Dec 27	3	26	5	12
2014 Dec 28	3	26	5	12
2015 Nov 5	2	6	3	11
2015 Nov 6	2	6	3	11
2015 Dec 13	4	10	5	13
2016 Aug 4 (<i>R</i> band)	3	11	5	21
2016 Aug 5 (<i>R</i> band)	3	11	5	21;8‡
2016 Aug 5 (<i>V</i> band)	6	30	5	8‡
2016 Aug 6 (<i>R</i> band)	3	11	5	21
2016 Aug 7 (<i>R</i> band)	3	11	5	21
2016 Aug 7 (<i>V</i> band)	7	22	5	8‡
2016 Aug 8 (<i>R</i> band)	3	11	5	21
2016 Aug 8 (<i>V</i> band)	5	22	5	8‡

†Landolt standard stars: PG2213+006a, PG2213+006b and PG2213+006c.

‡Landolt standard stars: SA23_435, SA23_438, SA23_443, SA23_444, SA23_440, SA23_433.

Table 5. Photometry results for the observations from the Calar Alto, Roque de los Muchachos and Sierra Nevada observatories. We list the Julian Date (JD, corrected from light time); the relative magnitude (Rel. mag., in mag); the error associated (Err. in mag); the topocentric (*r*_H) and heliocentric (Δ) distances (both distances expressed in au) and the solar phase angle (α , in deg). The full table is available online.

JD	Rel. Mag. (mag)	Err. (mag)	<i>r</i> _H (au)	Δ (au)	α (°)
2456980.16349	−0.0065	0.0243	16.042	15.169	1.699
2456980.16866	−0.0175	0.0301	16.042	15.169	1.699
2456980.17227	−0.0312	0.0230	16.042	15.169	1.699
2456980.17587	−0.0099	0.0176	16.042	15.169	1.699
2456980.17948	−0.0705	0.0277	16.042	15.169	1.699
2456980.18309	−0.0432	0.0265	16.042	15.169	1.700
2456980.18669	0.0023	0.0217	16.042	15.169	1.700

to similar magnitude stars. This step enabled us to assess the quality of the photometric measurement. The number of reference stars can be seen in Table 4. From the campaigns three different light curves were obtained. Photometry results are given in Table 5.

From the data, we determined our own rotational period of 9.1713 ± 0.0011 h that is consistent within the error bars with that determined by Rabinowitz, Schaefer & Tourtellotte (2007) and Ortiz et al. (2002). We folded the photometric data taken in 2014, 2015 and 2016 using this rotational period. In order to calculate the light-curve amplitude, we fitted the data points to a second-order Fourier function as follows:

$$m(\phi) = a_0 + a_1 \cos(2\pi\phi) + b_1 \sin(2\pi\phi) + a_2 \cos(4\pi\phi) + b_2 \sin(4\pi\phi), \quad (1)$$

where $m(\phi)$ is the relative magnitude given by the fit to this equation, ϕ is the rotational phase and a_0 , a_1 , a_2 , b_1 and b_2 are the

Table 6. Parameters for the second-order Fourier function fits for 2014, 2015 and 2016 light curves. Columns are as follows: arbitrary initial Julian date (J_{D_0}), second-order Fourier function coefficients (a_0 , a_1 , a_2 , b_1 and b_2) and Pearson's χ^2 per degree of freedoms test (χ^2_{pdf}).

Run	J_{D_0}	a_0	a_1	a_2	b_1	b_2	χ^2_{pdf}
2014	2456980.0	−0.007 610 12	−0.009 935 54	−0.032 113 67	−0.016 948 34	0.015 6932	1.55
2015	2456980.0	−0.015 637 93	−0.001 617 43	−0.020 891 69	−0.023 635 07	0.014 272 25	1.24
2016	2456980.0	0.003 642 51	0.023 303 65	0.012 344 25	−0.026 998 05	0.013 381 58	1.77

Fourier coefficients (see Table 6). Rotational phase is given by the following equation: $\phi = (J_D - J_{D_0})/P$, where $J_{D_0} = 2456980$ is an arbitrary initial Julian date corrected for light travel time, P is the target's rotational period in days and J_D is the Julian date corrected from light travel time. We obtained three light-curve amplitude values: $\Delta m = 0.088 \pm 0.008$ mag, $\Delta m = 0.082 \pm 0.007$ and $\Delta m = 0.10 \pm 0.02$ mag for the 2014, 2015 and 2016 light curves, respectively. These three light curves can be seen in Figs 1a, 1b and 1c.

Finally, in order to check the quality of the photometric analysis of the object, the dispersion of the residual of the fit to equation (1) was compared with the dispersion of the measurements of a star of similar flux or slightly lower than Bienor's flux (see Table 7). In order to minimize the dispersion caused by external factors, such as different CCDs or large temporal distances between observation campaigns, only those days sharing the same reference stars and also the same telescope were used for the purpose of comparing the fluxes. Therefore, only data obtained at NOT were used in the 2014 run; similarly, data obtained in November at CAHA 1.23 m were used in the 2015 run. In order to obtain the dispersion of the star, the relative magnitude was calculated with respect to the remaining reference stars. The dispersion value of the residual fit to the Fourier function is bigger in both rotational light curves in years 2014 and 2015 than the dispersion of the control star for each run. The slightly larger dispersion of Bienor's residuals compared to the dispersion of control stars may indicate a slight deficiency of the light-curve modelling or intrinsic variability of Bienor at the level of ~ 0.004 mag. Note that the dispersion of the data in 2016 was significantly higher than in 2014 and 2015; therefore, no clear conclusion in this regard can be obtained from the 2016 data.

3.2 Absolute magnitude

The absolute magnitude of a Solar system body is defined as the apparent magnitude that the object would have if located at 1 au from the Sun, 1 au from the Earth and with 0° phase angle. This magnitude is obtained from the well-known equation:

$$H = m_{\text{Bienor}} - 5 \log(r_H \Delta) - \phi(\alpha), \quad (2)$$

where H is the absolute magnitude of Bienor, m_{Bienor} is the apparent magnitude of Bienor, r_H is the heliocentric distance, Δ is the topocentric distance and $\phi(\alpha)$ is a function that depends on the phase angle. This function can be approximated by $\alpha\beta$, where α is the phase angle and $\beta = 0.1 \pm 0.02$ mag deg $^{-1}$ is the phase correction coefficient, which is the average value from β_V and β_I given by Rabinowitz et al. (2007). This value agrees with the value obtained in the phase angle study of Alvarez-Candal et al. (2016). On the other hand, the apparent magnitude of Bienor is given as follows:

$$m_{\text{Bienor}} = m_{\star i} - \frac{5}{2} \log \left(\frac{\langle F_{\text{Bienor}} \rangle}{\langle F_{\star i} \rangle} \right) - k \Delta \zeta, \quad (3)$$

where $m_{\star i}$ is the apparent magnitude of Landolt standard stars (the subscript i indicates different Landolt standard stars); $\langle F_{\text{Bienor}} \rangle$ is the average flux of Bienor; $\langle F_{\star i} \rangle$ is the average flux of different Landolt standard stars; k is the extinction coefficient and $\Delta \zeta$ is the difference between the Landolt standard stars' air mass and Bienor's air mass.

We carried out a linear fit in order to obtain the extinction coefficient following the equation:

$$m_{\star, i} = m_{\star, i}^0 + k \zeta, \quad (4)$$

where $m_{\star, i}$ is the apparent magnitude of the star and $m_{\star, i}^0$ is the apparent magnitude corrected for atmospheric extinction (see Table 8).

Finally, the values obtained for the absolute magnitudes of Bienor, during the 2013 campaign, in V and R band are 7.42 ± 0.05 mag and 7.00 ± 0.05 mag, respectively. On the other hand, the absolute magnitudes, during the 2016 campaign, in V and R band are 7.47 ± 0.04 mag and 7.03 ± 0.02 mag. From those, we could also obtain the $(V - R)$ colour, which is 0.42 ± 0.07 mag and 0.44 ± 0.07 mag in 2013 and 2016, respectively.

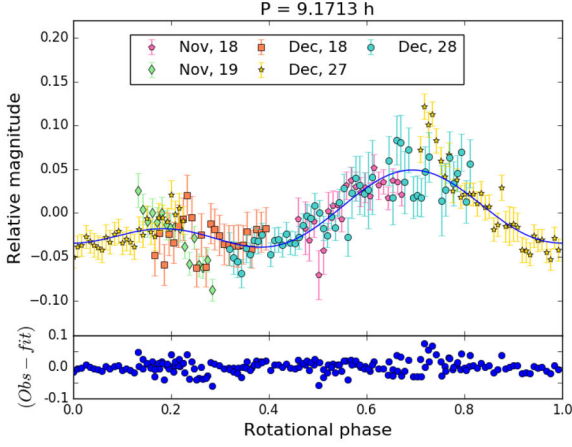
4 SIMPLE ELLIPSOID DESCRIPTION

4.1 Pole determination (modelling of the light-curve amplitude)

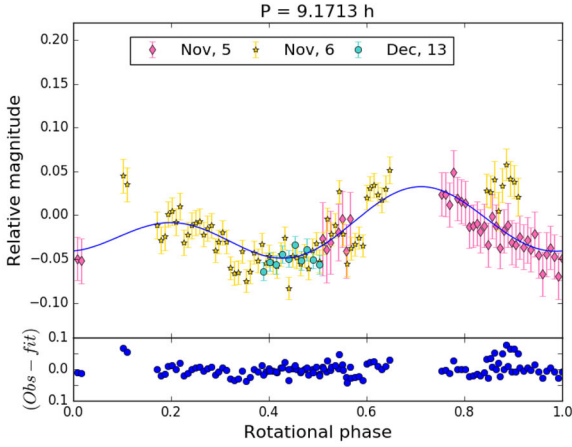
As can be seen in Table 9, the light-curve amplitude has changed within the last 16 yr from 0.609 mag (Ortiz et al. 2002)¹ in 2000 to 0.082 mag in 2015 and actually it seems that it is starting to increase slightly (this work, Section 3.1). This implies that Bienor's aspect angle is evolving in time. We can take advantage of this to determine the orientation of the pole of the centaur as first done in Tegler et al. (2005) for centaur Pholus. We consider that Bienor is a Jacobi ellipsoid as in previous works (Ortiz et al. 2002; Rabinowitz et al. 2007). Furthermore, as shown in the three rotational light curves (Figs 1a, 1b and 1c) and in rotational light curves published in the aforementioned works, the maxima and minima of the Fourier function have different depths, which is another indication that the light curve is indeed mainly due to the body shape. The light-curve amplitude produced by a triaxial body shape is given by the following equation:

$$\Delta m = -2.5 \log \left(\frac{A_{\min}}{A_{\max}} \right), \quad (5)$$

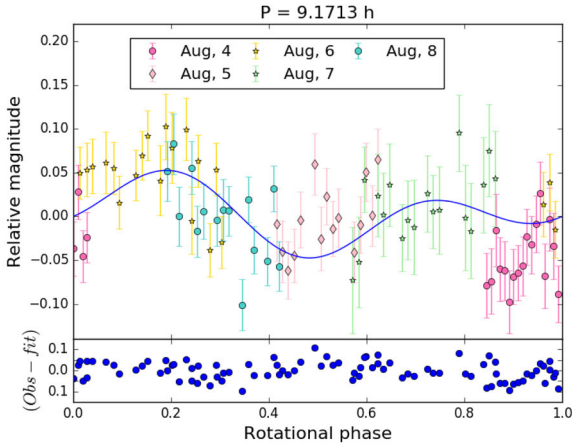
¹ We took the data published in that work to fit to a Fourier function as in Section 3.1 to determine our own Δm value, which is slightly lower than that reported by Ortiz et al. (2002). This is because those authors took just the maximum and minimum of their data and subtracted them.



(a) Rotational light curve from 18th and 19th November and from 18th, 27th and 28th December 2014.



(b) Rotational light curve from 5th and 6th November and 13th December 2015.



(c) Rotational light curve from 4th to 8th August 2016.

Figure 1. Rotational light curves from 2014 (upper panel), 2015 (middle panel) and 2016 (bottom panel). The points represent the observational data, each colour and symbol corresponding to a different day. The blue line shows the fit of the observational data to the second-order Fourier function (equation 1). At the bottom of each panel, it can be seen the residual values of the second-order Fourier function fit to the observational data.

Table 7. Comparison between the dispersion of the fit residual to the Fourier function and the dispersion of the star data with similar or lower flux than Bienor flux. Abbreviations are defined as follows: dispersion of the fit residual to the Fourier function (σ_{Bienor}) and dispersion of the star residual (σ_*).

Campaign	σ_{Bienor}	σ_*
2014	0.020	0.016
2015	0.022	0.010
2016	0.050	0.040

where A_{\min} and A_{\max} are the minimum and maximum area of the object given by

$$A_{\min} = \pi b [a^2 \cos^2(\delta) + c^2 \sin^2(\delta)]^{1/2} \quad (6)$$

and

$$A_{\max} = \pi a [b^2 \cos^2(\delta) + c^2 \sin^2(\delta)]^{1/2}, \quad (7)$$

where a , b and c are the semi-axes of the triaxial body (with $a > b > c$). Semi-axes ratios can be estimated under the assumption of hydrostatic equilibrium (Chandrasekhar 1987) and should comply with the fact that the effective diameter (in area) is 198_{-7}^{+6} km as determined by *Herschel* measurements (Duffard et al. 2014a). Finally, δ is the aspect angle, which is given by the ecliptic coordinates of the angular velocity vector (the pole direction) and the ecliptic coordinates of the object as follows:

$$\delta = \frac{\pi}{2} - \arcsin [\sin(\beta_e) \sin(\beta_p) + \cos(\beta_e) \cos(\beta_p) \cos(\lambda_e - \lambda_p)], \quad (8)$$

where β_e and λ_e are the ecliptic latitude and longitude of the sub-Earth point in the Bienor-centred reference frame and β_p and λ_p are the ecliptic latitude and longitude of Bienor's pole (Schroll, Haupt & Maitzen 1976).

We fitted the observational data from the literature and this work (see Table 9) to the equation (5). We carried out a grid search for the quantities β_p , λ_p and b/a axis ratio, which gave theoretical values for Δm with the smallest χ^2 fit to the observed points. β_p and λ_p were explored on the entire sky at intervals of 5° , and b/a ratio was explored from 0.33 to 0.57 at steps of 0.04. The limiting values defining this interval, 0.33 and 0.57, are chosen taking into account that relation between the b/a and the light-curve amplitude of the object. On the one hand, the upper limit $b/a = 0.57$ is determined by the maximum light-curve amplitude observed for Bienor up to date (Ortiz et al. 2003), namely the first point in Fig. 2 from year 2001. The measured amplitude implies that b/a cannot be below 0.57, as lower ratios would fail to provide such a rotational variability, independently of the value of the aspect angle. On the other hand, the lower limit gives $b/a = 0.33$ from the condition that the light-curve amplitude is always below $\Delta m = 1.2$ mag. Light-curve amplitudes that go above this value at some point in the evolution of the object are most likely caused by contact binary systems (Leone et al. 1984).

In order to evaluate the goodness of the fit, we used a χ^2 test as follows:

$$\chi^2_{\Delta m} = \frac{\sum ((\Delta m_{\text{theo}} - \Delta m_{\text{obs}})^2 / e_{\Delta m}^2)}{N_{\Delta m}}, \quad (9)$$

where Δm_{theo} represents theoretical values, Δm_{obs} represents observational data, $e_{\Delta m}$ represents errors for light-curve amplitude

Table 8. Absolute photometry results for the observations from the OSN. We list the Julian Date (J_D); the filter in the Bessell system; the absolute magnitude (H , in mag); the error associated with the absolute magnitude (e_H , in mag); the extinction coefficient (k); the error associated with the extinction coefficient (e_k); the air mass (ζ); the topocentric (r_H) and heliocentric (Δ) distances (both distances expressed in au) and the solar phase angle (α , in deg).

J_D	Filter	H (mag)	e_H (mag)	k	e_k	ζ	r_H (au)	Δ (au)	α ($^\circ$)
2456572.43011	V	7.42	0.05	0.30	0.02	1.15	16.395	15.4756	1.4108
2456572.45304	R	7.00	0.02	0.37	0.02	1.09	16.395	15.4756	1.4108
2457606.60204	V	7.46	0.09	0.09	0.05	1.68–1.14	15.496	15.558	3.7375
2457606.60204	R	7.03	0.02	0.06	0.04	1.65–1.16	15.496	15.558	3.7375
2457608.58729	V	7.49	0.08	0.12	0.05	2.03–1.12	15.494	15.545	3.7322
2457609.60545	V	7.46	0.03	0.08	0.04	1.53–1.12	15.494	15.508	3.7489

Table 9. Bienor’s light-curve amplitudes from different epochs.

Date (yr)	2001.626	2004.781	2014.930	2015.951	2016.597
Δm (mag)	0.609 ± 0.048^a	0.34 ± 0.08^b	0.088 ± 0.007^c	0.082 ± 0.009^c	0.10 ± 0.02^c

^aOrtiz et al. (2003). ^bRabinowitz et al. (2007). ^cThis work.

observational data and $N_{\Delta m}$ is the number of the light-curve amplitude observational data.

The result was a pole solution of $\beta_p = 50 \pm 3^\circ$ and $\lambda_p = 35 \pm 8^\circ$ and axes ratio of $b/a = 0.45 \pm 0.05$ (see Table 10). These values gave a $\chi^2_{\Delta m}$ of 0.27 (the direction $\lambda_p = 215^\circ$ and $\beta_p = -50^\circ$ is also possible for the same $\chi^2_{\Delta m}$ value). In Fig. 2, the blue line represents the light-curve amplitude model; also the observational data are shown. To estimate the uncertainties, we searched for all parameters within $\chi^2_{\Delta m, \min}$ and $\chi^2_{\Delta m, \min} + 1$.

4.2 Modelling of the absolute magnitude

Right from the first observing runs that we carried out, we realized that the amplitude of the rotational variability of Bienor had changed dramatically with respect to the first measurements in 2001, in which the amplitude was around 0.7 mag (Ortiz et al. 2003). The usual explanation to that kind of changes in Solar system bodies is related to a change in orientation of an elongated body. As explained in the previous section, using that approach for Bienor we came up with reasonable results. However, as discussed in the following, this kind of model does not offer a satisfactory explanation of the large change in the absolute magnitude of Bienor in the last 16 yr, which is considerably larger than what would be expected. In Table 11, we show absolute magnitudes from the literature and from this work.

The absolute magnitude of Bienor can be obtained using the previous values of the three parameters (β_p , λ_p and b/a) by means of the following equation:

$$H_V = -V_\odot + 2.5 \log \left(\frac{C^2 \pi}{p_V A_B(\delta)} \right), \quad (10)$$

where H_V is the absolute magnitude of the object, $V_\odot = -26.74$ mag is the absolute magnitude of the Sun in V band, $p_V = 0.043^{+0.016}_{-0.012}$ is the geometric albedo of the object in V band (Duffard et al. 2014a), $C = 1.496 \times 10^8$ km is a constant and $A_B(\delta)$ is the rotational average area of the body in km^2 , as determined from A_{\min} and A_{\max} given by equations (6) and (7), respectively, with the constraint that the mean area matches the area for Bienor’s effective diameter of 198^{+6}_{-7} km determined by *Herschel* (Duffard et al. 2014a).

This can be compared with the observational data shown in Table 11, as illustrated in the blue line in Fig. 3. It is apparent

that the absolute magnitude observational data do not follow the curve obtained from equation (10). Indeed, we obtained a value of 195 for the χ^2 test, which now is defined as follows:

$$\chi^2_{H_V} = \frac{\sum \left((H_{V, \text{theo}} - H_{V, \text{obs}})^2 / e_{H_V}^2 \right)}{N_{H_V}}, \quad (11)$$

where $H_{V, \text{theo}}$ represents theoretical absolute magnitudes, $H_{V, \text{obs}}$ represents observational data, e_{H_V} represents errors for absolute magnitude observational data and N_{H_V} is the number of the absolute magnitude observational data.

5 MORE COMPLEX MODELS

5.1 Simultaneous modelling of absolute magnitude and light-curve amplitude (HE model)

Given this situation, one might wonder whether it would be possible to find a set of values for the parameters β_p , λ_p and b/a axis ratio, leading to a satisfactory fit for both equations (5) and (10) simultaneously. To check the viability of this possibility, we defined a χ^2_T value so as to evaluate both fits at the same time as follows:

$$\chi^2_T = \frac{(\chi^2_{\Delta m} + \chi^2_{H_V})}{2}. \quad (12)$$

Here, $\chi^2_{\Delta m}$ is the χ^2 value from equation (9) and $\chi^2_{H_V}$ is the χ^2 value from equation (11). The χ^2_T value obtained using the original values of the parameters (β_p , λ_p and b/a) as in the previous section was ~ 98 . We searched for other sets of values that could fit satisfactorily both equations; nevertheless, all possible parameters gave poor fits with $\chi^2_T > 45$.

Hence, we did not find any solution that can fit satisfactorily the observational data of the absolute magnitude. As shown in Fig. 3, there is an increase of brightness with time that is not explained by the *hydrostatic model*. This leads us to think that there must be some physical process that produces such a large slope in the observational data, which we are not taking into account. This physical process might have to do with the existence of material orbiting around Bienor with a ring shape. The reflected flux contribution due to a ring plus the reflected flux contribution due to the body, as in the cases of Chariklo and Chiron (Braga-Ribas et al. 2014;

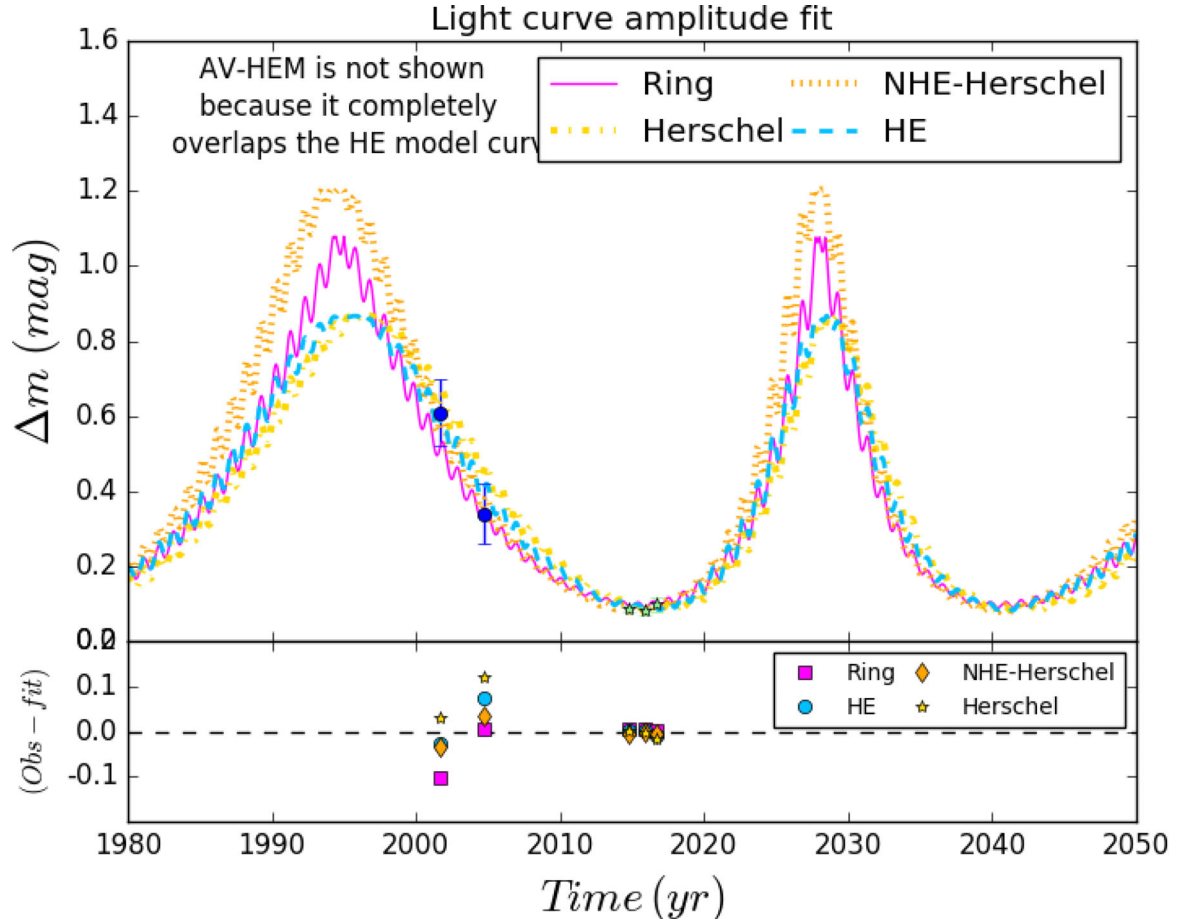


Figure 2. Bienor’s light-curve amplitude fit. At the top panel: the blue dashed line represents the hydrostatic equilibrium model (*HE* model, see Section 4.1). The pink line represents the ring system model (*ring* model, see Section 5.5). The yellow dotted line represents the hydrostatic equilibrium model relaxing *Herschel* constraints (*Herschel* model, see Section 5.2). The orange dotted line represents the no hydrostatic equilibrium model relaxing *Herschel* constraints (*NHE-Herschel* model, see Section 5.3). Dark blue circle points show data taken from literature. Green star points show data from this work. Bottom panel: residuals of the observational data with respect to the different models. Blue circle points correspond to the hydrostatic equilibrium model. Pink square points correspond to the ring system model. Yellow star points correspond to the hydrostatic equilibrium model relaxing *Herschel* constraints. Orange diamond points correspond to the no hydrostatic equilibrium model relaxing *Herschel* constraints. *Albedo* model is not shown because it completely overlaps the *HE* model curve.

Table 10. Results from the simplest modelling of the light-curve amplitude (see Section 4.1). Columns are as follows: elongation (b/a); flattening (c/b), ecliptic latitude and longitude of Bienor’s pole (β_p , λ_p), χ^2 test from equation (9) ($\chi^2_{\Delta m}$).

b/a	c/b	β_p ($^\circ$)	λ_p ($^\circ$)	ρ (kg m^3)	$\chi^2_{\Delta m}$	n	N
0.45 ± 0.05	0.79 ± 0.02	50 ± 3	35 ± 5	594^{+47}_{-35}	0.27	3	5

Note that the $\beta_p = -50^\circ$ and $\lambda_p = 215^\circ$ solution is also valid.

Ortiz et al. 2015), could produce the strong drop that is shown in the observational data of the absolute magnitude (see Section 5.5). However, other scenarios might be also possible. In the following, we discuss the different scenarios that we have considered.

5.2 Modelling of the data relaxing both the albedo and the effective diameter constraints from *Herschel* (*Herschel* model)

If one takes a look at the absolute magnitude plot, it seems like the model in blue in Fig. 3 is displaced up with respect to the data points. This means that the albedo or the effective diameter could

be higher than we used for the model, or even a combination of both of them. Therefore, we search around the values given by Duffard et al. (2014a) taking into account their error bars. As a result, the fit was improved using an albedo of 5.7 per cent and an effective diameter of 204 km (see yellow line in Fig. 3). This last fit modifies slightly the pole direction obtained in Section 4.1 (see Table 12, this model is referred to as *Herschel*). However, the model is still poor and does not represent the drop of the observational points.

5.3 Modelling of the data relaxing the assumption of hydrostatic equilibrium (*NHE* model)

We thought about the possibility that Bienor might not be in perfect hydrostatic equilibrium; this is possible because Bienor’s size is small enough to allow for departures of hydrostatic equilibrium. Therefore, we also searched the aforementioned grid adding the c/b axis ratio from 0.5 to 1.0 at intervals of 0.1. The smallest χ^2 , which was equal to 13.63, provides us the following parameters: 60° , 25° , 0.33 and 0.5 for β_p , λ_p , b/a and c/b , respectively. However, these ratios imply an extremely elongated body with an a -axis around six times bigger than the c -axis. There is no known body in the Solar

Table 11. Bienor’s absolute magnitude in different epochs. Abbreviations are as follows: absolute magnitude in V band (H_V), its associated error reported by the authors (e_{H_V}) and modified errors that we estimate as described in the Section 6 (e'_{H_V}). The renormalization of the uncertainties bias the fit towards most recent values, as light-curve amplitudes are smaller in recent epochs.

Observation date	H_V (mag)	e_{H_V} (mag)	e'_{H_V} (mag)	Bibliography
2000 Nov.	8.08	0.06	0.31	Delsanti et al. (2001)
2001 May	7.75	0.02	0.26	Tegler, Romanishin & Consolmagno (2003)
2002 ^b	7.85 ^a	0.05	0.26	Bauer et al. (2003)
2002 Aug.	8.04	0.02	0.22	Doressoundiram et al. (2007)
2004 ^c	7.588	0.035	0.035	Rabinowitz et al. (2007)
2007 Sep.	7.46	0.03	0.13	DeMeo et al. (2009)
2013 Oct.	7.42	0.02	0.04	This work
2016 Aug.	7.47	0.04	0.04	This work

Notes. Doressoundiram et al. (2002) published another value of Bienor’s magnitude that is in disagreement with the value for the same epoch published by Tegler et al. (2003). In order to check the correct value, we searched for other values in the Minor Planet Center data base for the same epoch. We found reliable data from surveys in Johnson’s R and V band that were in agreement with Tegler et al. (2003) but not with Doressoundiram et al. (2002). For this reason, we have not included the Doressoundiram et al. (2002) data point.

^aValue obtained from absolute magnitude in the R band using the colour correction published by the authors.

^bBauer et al. (2003) observed Bienor on 2001 October 29 and on 2002 June 13.

^cRabinowitz et al. (2007) observed Bienor between 2003 July and 2005 December.

system with this extremely elongated shape for such a large body as Bienor. Hence, we do not think that this is plausible. This model is referred to as *NHE* in Table 12.

However, we tried to find a good fit simultaneously relaxing the *Herschel* constraints as in the last subsection. This search provides a possible solution for an albedo of 5.1 per cent and using the effective diameter given by *Herschel* with a pole direction of 50° , 30° for β_p , λ_p , respectively, and axis ratio of 0.33 and 0.7 for b/a and c/b , respectively. This model is plotted in Figs 2 and 3 (see orange line) and referred as *NHE–Herschel* model in Table 12.

5.4 Modelling of the data with the inclusion of variable geometric albedo (*albedo* model)

Another possibility to increase the brightness of Bienor beyond the values of the modelling in Section 4.2 is to increase the geometric albedo of the body as a function of time or as a function of aspect angle. If the polar regions of Bienor have very high albedo, then it might be possible that Bienor becomes brighter as seen from Earth simply because we observe higher latitudes of Bienor as the aspect angle changes (because the current aspect angle in 2015 is $\sim 150^\circ$, see Fig. 4). The needed change of Bienor’s geometric albedo is from 3.9 per cent in 2000 to 7.6 per cent in 2008, when the aspect angle is 100° and 130° , respectively. This is shown in Fig. 3 (green line). Following this situation, one can extrapolate the albedo that the object would have if its aspect angle is 180° . Under this assumption, the albedo should be around 10 per cent. Such a dramatic change in Bienor’s geometric albedo is hard to explain because the polar caps would have to have an even higher albedo than 10 per cent (which is the hemispheric average). For instance, a polar cap covering around 42 per cent of the total area (viewed from the top) with an albedo of 16 per cent would fit the data. A more confined polar cap would have to have an even higher albedo than 16 per cent. It is difficult to find a mechanism that would cause such a large north–south asymmetry on the surface. For reference, the maximum longitudinal albedo variability on Bienor is only around

a few percentage because the two maxima of the rotational light curve differ by only 0.05 mag. We refer to this model as *albedo* model in Table 12.

5.5 Modelling of the data with the inclusion of a ring system (*ring* model)

In order to explain the observational data of the absolute magnitude, we included a ring contribution in the aforementioned equations: (5) and (10), see Section 8. On the one hand, the light-curve amplitude produced by the system Bienor + ring, Δm_S , is now given as follows:

$$\Delta m_S = -2.5 \log \left(\frac{A_{\min} p_B + A_R p_R}{A_{\max} p_B + A_R p_R} \right). \quad (13)$$

The additional parameters are the ring’s area (A_R), the ring’s albedo (p_R) and Bienor’s albedo (p_B). A_R is given by

$$A_R = \pi \mu ((R_R + d_R)^2 - R_R^2), \quad (14)$$

where $\mu = |\cos(\delta)|$ (δ is the aspect angle, see Section 8); R_R is the ring’s radius and d_R is the ring’s width. On the other hand, the absolute magnitude of the system, H_S , is now given as follows:

$$H_S = -V_\odot + 2.5 \log \left(\frac{C^2 \pi}{A_B p_B + A_R p_R} \right). \quad (15)$$

The same exercise as in Section 4.1 was carried out. We explored the quantities λ_p , β_p , a/b , p_B , p_R , A_R and R_{eff} (Bienor’s effective radius) in equations (13) and (15) that gave theoretical values for both fits, light-curve amplitude and absolute magnitude, which minimize the difference between observational and theoretical data. A_R was explored from 4000 to 10 000 km² at intervals of 500 km², the effective radius from 90 to 99 km at intervals of 3 km. We also explored ring’s albedo from 8 to 16 per cent at steps of 2 per cent and Bienor’s albedo from 3 to 6 per cent at steps of 1 per cent. We should take into account that the solution of this problem is degenerated as different ring sizes combined with different nucleus

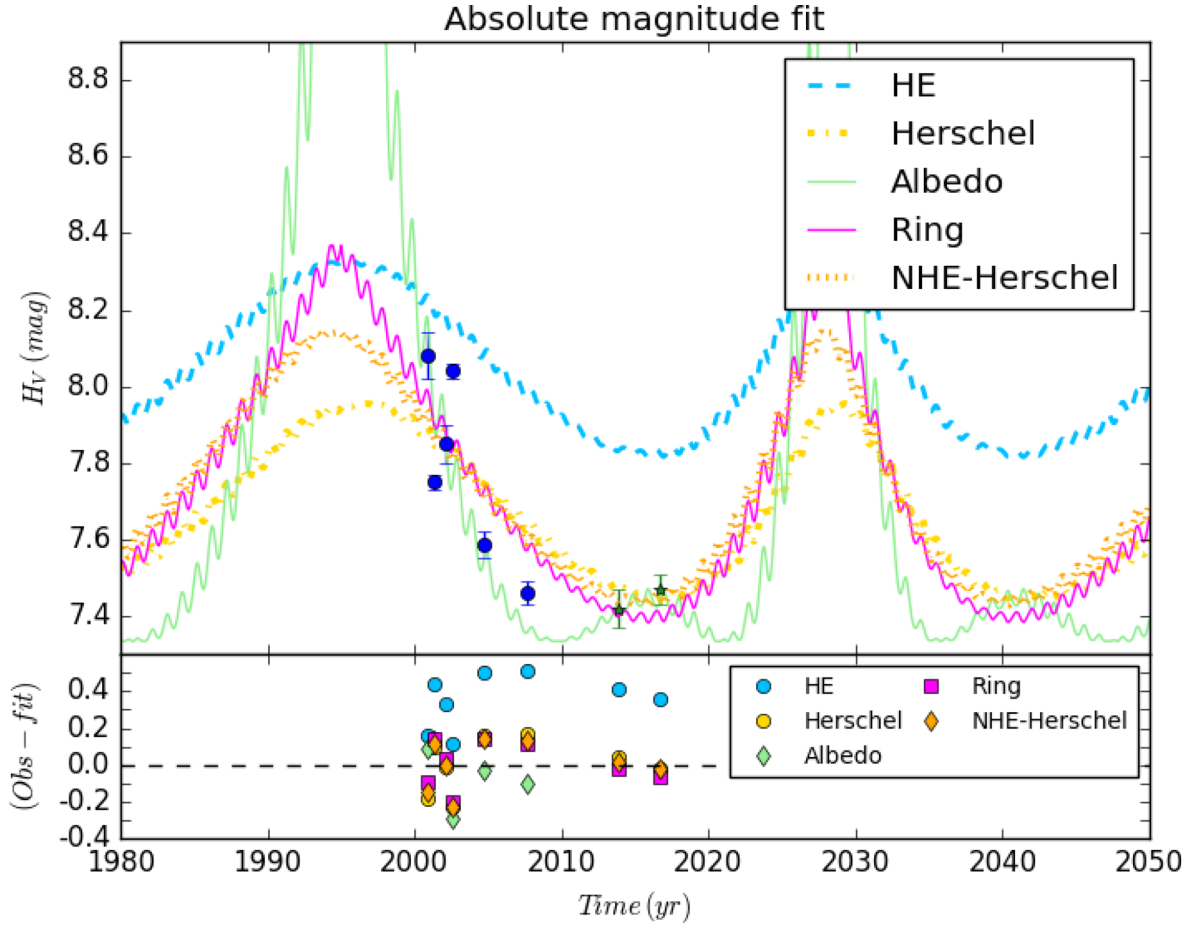


Figure 3. Bienor's absolute magnitude fit. The blue dashed line represents the hydrostatic equilibrium model (*HE* model, see Section 4.1). The pink line represents the ring system model (*ring* model, see Section 5.5). The yellow dotted line represents the hydrostatic equilibrium model relaxing *Herschel* constraints (*Herschel* model, see Section 5.2). The orange dotted line represents the no hydrostatic equilibrium model relaxing *Herschel* constraints (*NHE-Herschel* model, see Section 5.3). The green line represents the albedo variability model (*Albedo* model, see Section 5.4). The dark blue circle points show data taken from literature with errors reported by the authors. Green star points show data from this work. At the bottom panel: residual of the observational data. Blue star points correspond to the hydrostatic equilibrium model. Pink square points correspond to the ring system model. Yellow circle points correspond to hydrostatic equilibrium model relaxing *Herschel* constraints. Orange diamond points correspond to no hydrostatic equilibrium model relaxing *Herschel* constraints. Green diamond points represent albedo variability model.

Table 12. Bienor's parameters for each model to simultaneously fit light-curve amplitudes and absolute magnitudes using errors reported by the authors. The columns contain the following information: model designation (see foot note); elongation (b/a); flattening (c/b); ecliptic latitude and longitude of Bienor's pole (λ_p, β_p); Bienor's albedo in V band (p_B); Bienor's effective diameter (D_{eff}); ring's area (A_R); ring's albedo in V band (p_R); goodness of the fit given by the equation (9) ($\chi^2_{\Delta m}$); goodness of the fit given by the equation (11) (χ^2_H); goodness of the simultaneous fit to the equations (9) and (11) (χ^2_T); number of parameters of the fit (n); number of light-curve amplitude and absolute magnitude data ($N_{\Delta m}, N_H$).

Model	b/a	c/b	β_p ($^\circ$)	λ_p ($^\circ$)	p_B (per cent)	D_{eff} (km)	A_R (km 2)	p_R (per cent)	ρ (kg m $^{-3}$)	χ^2_T	$\chi^2_{\Delta m}$	χ^2_H	n	$N_{\Delta m}$	N_H
<i>HE</i>	0.33 ± 0.02	0.85 ± 0.01	25 ± 7	15 ± 6	$4.3^{+1.2}_{-1.6}$	198^{+6}_{-7}			742^{+41}_{-35}	45.3	18.8	71.8	3	5	7
<i>Herschel</i>	0.45 ± 0.08	0.79 ± 0.04	50 ± 4	40 ± 7	5.7 ± 0.2	204 ± 4			594^{+84}_{-52}	14.08	0.66	27.5	5	5	7
<i>NHE</i>	0.33 ± 0.03	0.5 ± 0.04	60 ± 5	25 ± 5	$4.3^{+1.2}_{-1.6}$	198^{+6}_{-7}				13.63	1.52	25.7	4	5	7
<i>NHE-Herschel</i>	0.33 ± 0.05	0.7 ± 0.05	50 ± 3	30 ± 6	5.1 ± 0.2	198 ± 3				12.69	0.23	25.2	6	5	7
<i>Albedo</i>	0.45 ± 0.09	0.79 ± 0.04	50 ± 3	35 ± 3	$3.9 - 7.6$	198^{+6}_{-7}			594^{+98}_{-57}	17.07	0.27	33.9	4	5	7
<i>Ring</i>	0.37 ± 0.10	0.83 ± 0.06	55 ± 3	30 ± 5	5.0 ± 0.3	180 ± 5	6000 ± 700	12.0 ± 1.5	678^{+209}_{-100}	12.40	0.40	24.4	7	5	7

HE: hydrostatic equilibrium model.

Herschel: hydrostatic equilibrium model relaxing *Herschel* constraints (Section 5.2).

NHE: no hydrostatic equilibrium mode (Section 5.3).

NHE-Herschel: no hydrostatic equilibrium model relaxing *Herschel* constraints (Section 5.3).

Albedo: albedo variability model (Section 5.4).

Ring: ring system model (Section 5.5).

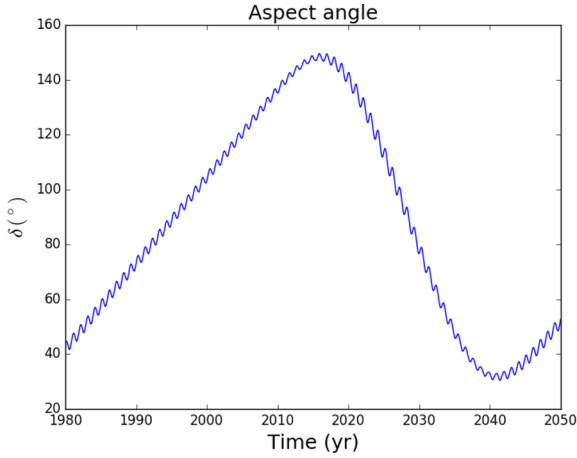


Figure 4. Bienor’s aspect angle versus time. The black line shows the result of the equation (8) with $\lambda_p = 35^\circ$ and $\beta_p = 50^\circ$. The edge-on position (when the angle between the spin axis orientation and the line of sight is 90°) is achieved around 1988 and around 2030.

sizes could fit to the data points. We just want to note that the ring solution is plausible. A hypothetical ring of around $10\,000\text{ km}^2$ is around two times smaller than Chiron’s ring as shown in Ortiz et al. (2015) and 1.2 times larger than that of Chariklo. A dense and narrow ring of 315-km inner radius and 318-km outer radius would do the job with no modification of the pole direction obtained in Section 4.1. The best fit for observational data provides the following values: $a/b = 0.37 \pm 0.10$, $p_B = 5.0 \pm 0.3$ per cent, $p_R = 12.0 \pm 1.5$ per cent, $A_R = 6000 \pm 700$ and $D_{\text{eff}} = 180 \pm 5$ km (see the pink lines in Figs 2 and 3). This is the best model in terms of χ^2_T . We refer to this model as *ring* model in Table 12.

6 DISCUSSION

We have considered several scenarios to simultaneously explain Bienor’s change of light-curve amplitude and absolute magnitude in the last 16 yr. As can be seen in Fig. 3, at least two of the models

seem to fit the data qualitatively, but the too high values of the goodness-of-fit test (Table 12) indicate that either the models are not fully satisfactory or that the errors have been underestimated. Indeed, we have reasons to suspect that the absolute magnitudes determined by several authors could have been affected by the large rotational variability of Bienor in those years. Hence, we revised the errors with the very conservative strategy of assigning an extra uncertainty of half the full amplitude of the rotational light curve at each epoch.

When the revised errors in Table 11 are used for the computation of new values of the goodness of fit, slightly different fits with respect to Table 12 are obtained. They are summarized in Table 13. Now the goodness-of-fit test provides too low values for some models, possibly indicating that the errors have been overestimated in this case. Given that an accurate determination of errors in the absolute magnitudes was not possible, we suspect that the reality probably falls in between the two different error estimates, and therefore the best model fits should be something in between the results of Tables 12 and 13.

As can be seen in aforementioned tables, *HE* model gives far poorer fits than the other models; therefore, we can conclude that a simple hydrostatic equilibrium model cannot fit the data. By relaxing the albedo and effective diameter constraints given by *Herschel* (Duffard et al. 2014a), we improved the fit. A better solution is found by relaxing both the assumption of hydrostatic equilibrium and *Herschel* constraints. But concerning this model, the main difficulty is that it requires a very extreme body with too large a/c ratio to be realistic for bodies of Bienor’s size. Nevertheless, there are models of dumb-bell-shaped contact binaries that can give rise to a/c axial ratios of up to 4.14 (Descamps 2015). Such a contact binary would not perfectly fit the data but together with a north–south asymmetry in the albedo might be close to offer a good solution. Using the formalism in Descamps (2015), the $a/c = 4.14$ axial ratio (approximately the axial ratio obtained in Section 5.3 when the *Herschel* constraints are relaxed) would require a density of 970 kg m^{-3} for Bienor, given its known 9.1713-h period. Such a density in TNOs is expected for objects with an effective diameter around 500 km (see supplementary material in Carry 2012;

Table 13. Bienor’s parameters for each model to simultaneously fit light-curve amplitudes and absolute magnitudes using errors taking into account the light-curve amplitude. The columns contain the following information: model designation (see foot note); elongation (b/a); flattening (c/b); ecliptic latitude and longitude of Bienor’s pole (λ_p , β_p); Bienor’s albedo in V band (p_B); Bienor’s effective diameter (D_{eff}); ring’s area (A_R); ring’s albedo in V band (p_R); goodness of the fit given by the equation (9) ($\chi^2_{\Delta m}$); goodness of the fit given by the equation (11) (χ^2_H); goodness of the simultaneous fit to the equations (9) and (11) (χ^2_T); number of parameters of the fit (n); number of light-curve amplitude and absolute magnitude data ($N_{\Delta m}$, N_H).

Model	b/a	c/b	β_p ($^\circ$)	λ_p ($^\circ$)	p_B (per cent)	D_{eff} (km)	A_R (km^2)	p_R (per cent)	ρ (kg m^{-3})	χ^2_T	$\chi^2_{\Delta m}$	χ^2_H	n	$N_{\Delta m}$	N_H
<i>HE</i>	0.33 ± 0.03	0.85 ± 0.02	40 ± 5	20 ± 9	$4.3^{+1.2}_{-1.6}$	198^{+6}_{-7}			742^{+64}_{-51}	16.4	4.18	28.7	3	5	7
<i>Herschel</i>	0.45 ± 0.07	0.79 ± 0.03	50 ± 3	35 ± 11	5.9 ± 0.6	204 ± 10			594^{+71}_{-47}	0.89	0.27	1.52	5	5	7
<i>NHE</i>	0.33 ± 0.05	0.5 ± 0.04	60 ± 3	25 ± 8	$4.3^{+1.2}_{-1.6}$	198^{+6}_{-7}				2.53	1.52	3.54	4	5	7
<i>NHE-Herschel</i>	0.33 ± 0.08	0.85 ± 0.07	45 ± 3	30 ± 7	5.9 ± 0.5	200 ± 8				0.58	0.28	0.89	6	5	7
<i>Albedo</i>	0.45 ± 0.07	0.79 ± 0.03	50 ± 3	35 ± 3	$3.9\text{--}7.6$	198^{+6}_{-7}			594^{+71}_{-47}	0.34	0.27	0.51	4	5	7
<i>Ring</i>	0.33 ± 0.12	0.85 ± 0.06	50 ± 5	25 ± 10	5.0 ± 0.5	192 ± 10	4000 ± 1300	12.0 ± 0.4	742^{+401}_{-149}	0.63	1.00	0.81	7	5	7

HE: hydrostatic equilibrium model.

Herschel: hydrostatic equilibrium model relaxing *Herschel* constraints (Section 5.2).

NHE: no hydrostatic equilibrium mode (Section 5.3).

NHE-Herschel: no hydrostatic equilibrium model relaxing *Herschel* constraints (Section 5.3).

Albedo: albedo variability model (Section 5.4).

Ring: ring system model (Section 5.5).

The χ^2_T values were obtained with the revised errors e'_{H_V} of Table 11.

Ortiz et al. 2012); such a diameter is 2.5 times bigger than Bienor's effective diameter. Nevertheless, 970 kg m^{-3} cannot be completely discarded.

Concerning the albedo variability model, this would require a very bright polar cap on Bienor whereas the equatorial parts would have a geometric albedo of only a few percentage. No centaur or small TNO has ever been found to exhibit such a remarkable albedo variability in its terrain. Polar caps of ices may be expected in objects with evaporation and condensation cycles, which does not seem to be viable for centaurs, because CO_2 would be too volatile and H_2O is not sufficiently volatile with the temperatures involved at the distances to the Sun in which Bienor moves. Hence, even though this is a possibility, it does not seem very promising.

For all of the above, we thought about the possibility that Bienor could have a ring system or a partial ring system because we know at least two other similar sized centaurs that have ring material around them (Braga-Ribas et al. 2014; Ortiz et al. 2015). When this possibility was considered, we got a slightly better solution than for the no hydrostatic equilibrium model relaxing the *Herschel* constraints, with no modification of the pole direction that was obtained from the light-curve amplitude fit in the case in which no ring is included (see Section 4.1).

On the other hand, we know that there is water ice detection in Bienor's spectra already reported in the literature (e.g. Dotto et al. 2003; Barkume, Brown & Schaller 2008; Guilbert et al. 2009), which would also be consistent with the idea that Bienor could have an icy ring or icy ring material around its nucleus. This has been the case for centaurs Chariklo and Chiron, which also have spectroscopic detection of water ice, and the variation of the depth of the ice features in their spectra is well explained due to a change in the aspect angle of the rings. This was a clear indication that the water ice is in the rings of these centaurs (Duffard et al. 2014b; Ortiz et al. 2015). Hence, the presence of water ice in the spectrum of centaur Bienor is also a possible indication of a ring around Bienor's nucleus. In fact, all centaurs that exhibit a water ice feature in their spectrum may be suspect of having a ring system.

Besides, the density we derive for Bienor with the model that includes a ring system (742 kg m^{-3} in Table 13, 678 kg m^{-3} in Table 12) is slightly higher than what we derive without the inclusion of a ring system (594 kg m^{-3} , see Table 12). The higher value looks somewhat more realistic because we already know (with high accuracy) the density of comet 67P from the Rosetta visit ($533 \pm 0.006 \text{ kg m}^{-3}$ according to Pätzold et al. 2016). It would be somewhat surprising that the density of Bienor, which is much larger than comet 67P would be nearly identical, as we expect less porosity for larger bodies (e.g. Carry 2012).

Therefore, the model with a ring not only explains the photometry but also results in a density value that seems more realistic. Hence, a putative ring offers a more consistent physical picture than a huge albedo north-south asymmetry in the surface of Bienor or the other models, although combinations of the three different scenarios discussed may also give a satisfactory fit to the data. Hence, even though we favour the possibility that Bienor could have ring system, it is not firmly proven.

Future stellar occultations by Bienor may ultimately confirm or reject the existence of a dense ring system. In this regard, there will be two potentially good stellar occultation by Bienor on 2017 February 13 and December 29. These are occultations of bright enough stars so that detection of ring features is feasible and occur in highly populated areas of the world. Observations of these events and other future stellar occultations by Bienor, as well as spectroscopic observations, will indeed be valuable.

It must be noted that the derivation of the spin axis direction is not highly dependent on the different models, so we have derived a relatively well-constrained spin axis direction of $\lambda_p = 25^\circ\text{--}40^\circ$ and $\beta_p = 45^\circ\text{--}55^\circ$. Note that the symmetric solution $\lambda_p = 25^\circ + 180^\circ$ to $40^\circ + 180^\circ$ and $\beta_p = -45^\circ$ to -55° is also possible. Besides, despite the different models, we have derived a well-constrained density between 550 and 1150 kg m^{-3} in the most extreme cases.

7 CONCLUSIONS

Thanks to several photometry runs in which we observed a remarkable change in the amplitude of the rotational variability of Bienor since 2000, and together with data available in the literature, we have been able to determine the orientation of the pole of Bienor ($\beta_p = 50^\circ$, $\lambda_p = 30^\circ$), and we have derived its shape ($b/a = 0.45$). These results, together with the known rotation period, allowed us to determine a density for Bienor of 594 kg m^{-3} under the usual assumption of hydrostatic equilibrium. However, we find that the absolute magnitude of Bienor observed in different epochs is not compatible with a simple triaxial ellipsoid shape. We have investigated several possible scenarios to explain the anomalous absolute magnitude decline. We find that the inclusion of a thin ring system can explain the observed variation although other scenarios cannot be discarded. The required ring system's albedo and width are similar to those found in Chariklo and Chiron. When the ring system is included, the shape of Bienor's nucleus has to be somewhat more elongated and the resulting density is in between 688 and 742 kg m^{-3} , slightly higher than in the case in which no ring is considered. Future stellar occultation may shed light on the possible existence of a ring. To put the results in context, density, shape and pole orientation are important physical parameters that have been determined for only three other centaurs.

ACKNOWLEDGEMENTS

We are grateful to the NOT, CAHA and OSN staffs. This research is partially based on observations collected at CAHA at Calar Alto, operated jointly by the Max-Planck Institut für Astronomie and the Instituto de Astrofísica de Andalucía (CSIC). This research was also partially based on observation carried out at the Observatorio de Sierra Nevada (OSN) operated by Instituto de Astrofísica de Andalucía (CSIC). This article is also based on observations made with the NOT, operated by the NOT Scientific Association at the Observatorio del Roque de los Muchachos, La Palma, Spain, of the Instituto de Astrofísica de Canarias. Funding from Spanish grant AYA-2014-56637-C2-1-P is acknowledged, as is the Proyecto de Excelencia de la Junta de Andalucía, J. A. 2012-FQM1776. RD acknowledges the support of MINECO for his Ramon y Cajal Contract. The research leading to these results has received funding from the European Union's Horizon 2020 Research and Innovation Programme under Grant Agreement no. 687378. We thank the referee Dr Benoit Carry for very helpful comments.

REFERENCES

- Alvarez-Candal A., Pinilla-Alonso N., Ortiz J. L., Duffard R., Morales N., Santos-Sanz P., Thirouin A., Silva J. S., 2016, *A&A*, 586, A155
- Barkume K. M., Brown M. E., Schaller E. L., 2008, *ApJ*, 135, 55
- Bauer J. M., Meech K. J., Fernández Y. R., Pittichova J., Hainaut O. R., Boehnhardt H., Delsanti A. C., 2003, *Icarus*, 166, 195
- Braga-Ribas F. et al., 2014, *Nature*, 508, 72
- Campo Bagatin A., Benavidez P. G., 2012, *MNRAS*, 423, 1254

- Carry B., 2012, *Planet. Space Sci.*, 73, 98
- Chandrasekhar S., 1987, *Ellipsoidal Figures of Equilibrium*. Dover Press, New York
- Delsanti A. C., Boehnhardt H., Barrera L., Meech K. J., Sekiguchi T., Hainaut O. R., 2001, *A&A*, 380, 347
- DeMeo F. E. et al., 2009, *A&A*, 493, 283
- Descamps P., 2015, *Icarus*, 245, 64
- Doressoundiram A., Peixinho N., de Bergh C., Fornasier S., Thébault P., Barucci M. A., Veillet C., 2002, *AJ*, 124, 2279
- Doressoundiram A., Peixinho N., Moullet A., Fornasier S., Barucci M. A., Beuzit J.-L., Veillet C., 2007, *AJ*, 134, 2186
- Dotto E., Barucci M. A., Boehnhardt H., Romon J., Doressoundiram A., Peixinho N., de Bergh C., Lazzarin M., 2003, *Icarus*, 162, 408
- Duffard R. et al., 2014a, *A&A*, 564, A92
- Duffard R. et al., 2014b, *A&A*, 568, A79
- Fernández-Valenzuela E., Ortiz J. L., Duffard R., Santos-Sanz P., Morales N., 2016, *MNRAS*, 456, 2354
- Guilbert A., Alvarez-Candal A., Merlin F., Barucci M. A., Dumas C., de Bergh C., Delsanti A., 2009, *Icarus*, 201, 272
- Horner J., Evans N. W., Bailey M. E., 2004a, *MNRAS*, 354, 798
- Horner J., Evans N. W., Bailey M. E., 2004b, *MNRAS*, 355, 321
- Hyodo R., Charnoz S., Ohtsuki K., Genda H., 2016, *Icarus*, 282, 195
- Jewitt D., Morbidelli A., Rauer H., 2008, *Trans-Neptunian Objects and Comets*. Springer, Berlin
- Leone G., Paolicchi P., Farinella P., Zappala V., 1984, *A&A*, 140, 265
- Ortiz J. L., Baumont S., Gutiérrez P. J., Roos-Serote M., 2002, *A&A*, 388, 661
- Ortiz J. L., Gutiérrez P. J., Casanova V., Sota A., 2003, *A&A*, 407, 1149
- Ortiz J. L. et al., 2012, *Nature*, 491, 566
- Ortiz J. L. et al., 2015, *A&A*, 576, A18
- Pan M., Wu Y., 2016, *AJ*, 821, 18
- Pätzold M. et al., 2016, *Nature*, 530, 63
- Rabinowitz D. L., Schaefer B. E., Tourtellotte S. W., 2007, *AJ*, 133, 26
- Romanishin W., Tegler S. C., 2005, *Icarus*, 179, 523
- Schroll A., Haupt H. F., Maitzen H. M., 1976, *Icarus*, 27, 147
- Tegler S. C., Romanishin W., Consolmagno G. J., 2003, *AJ*, 599, L49
- Tegler S. C., Romanishin W., Consolmagno G. J., Rall J., Worhatch R., Nelson M., Weidenschilling S., 2005, *Icarus*, 175, 390

SUPPORTING INFORMATION

Supplementary data are available at [MNRAS](https://www.mnras.org/onlineonly) online.

Table 5. Photometry results for the observations from the Calar Alto, Roque de los Muchachos and Sierra Nevada Observatories.

Please note: Oxford University Press is not responsible for the content or functionality of any supporting materials supplied by the authors. Any queries (other than missing material) should be directed to the corresponding author for this article.

This paper has been typeset from a \LaTeX file prepared by the author.